npj | quantum information

Article

Published in partnership with The University of New South Wales

https://doi.org/10.1038/s41534-025-00999-x

Spin-optomechanical cavity interfaces by deep subwavelength phonon-photon confinement

Hamza Raniwala[1] ✉, Pratyush Anand[1], Stefan Krastanov[2], Matt Eichenfield[3,4], Matthew Trusheim[1,5] & Dirk R. Englund[1] ✉

A central goal of quantum information science is transferring qubits between space, time, and modality. Spin-based systems in solids are promising quantum memories, but high-fidelity transfer of their quantum states to telecom optical fields remains challenging. Here, we introduce a phonon-mediated interface between spins in a diamond nanobeam optomechanical crystal and telecom optical fields by a simultaneous deep-subwavelength confinement of optical and acoustic fields with mode volumes $V_{mech}/\Lambda_p^3 \sim 10^{-5}$ and $V_{opt}/\lambda^3 \sim 10^{-3}$, respectively. This confinement boosts the spin-mechanical coupling rate of Group-IV silicon vacancy (SiV^-) centers by an order of magnitude to ~ 32 MHz while retaining high acousto-optical couplings. The optical cavity couples to the spin irrespective of the emitter's native excited states, avoiding spectral diffusion. Using Quantum Monte Carlo simulations, we estimate heralded entanglement fidelities exceeding 0.96 between two such interfaces. We anticipate broad utility beyond diamond emitter-telecom systems to most solid-state quantum memories.

The interaction of light with solid matter via radiation pressure forces is a remarkable phenomenon whose discovery dates back to the 17th century[1,2]. In recent decades, progress on understanding and engineering this light-matter interaction has produced groundbreaking experiments in cavity optomechanics, including laser feedback cooling[3], parametric light-matter processes in kg-scale[4] and picogram-scale[5–7] optomechanical systems, and laser cooling of mechanical modes to their ground state[7,8]. These quantum optics-like experiments have paved the way for optomechanical devices to be used in quantum transduction[9–13] and entanglement[14,15].

Solid-state vacancy-defect complexes are a developing technology that is complementary to cavity optomechanics. These complexes are atomic defects in dielectric media, such as diamond, that can be intentionally created in a dielectric lattice[16,17]. The free electron spin or nuclear spin of the resulting lattice vacancies can be coherently controlled as solid state quantum bits[16,18]. Additionally, research efforts demonstrating acoustic control of spin centers has opened the door to multi-modality quantum systems, such as spin-optomechanical interfaces[19–21]. These complex coupled systems can potentially allow for dark-state operation of spin centers, optical-to-spin quantum transduction, and new architectures for quantum repeaters in a quantum network.

Here, we propose a spin-optomechanical interface in diamond for strong coupling between the mechanical mode of an optomechanical resonator and an embedded group IV defect-vacancy complex. Our device introduces an optical resonance to ultra-small mechanical cavities previously used for spin interfacing[22]. By jointly confining the optical (mechanical) mode to a normalized mode volume of $(10^{-3}\lambda^3\ (10^{-5}\Lambda_p^3)$, where λ (Λ_p) is the optical (longitudinal acoustic) wavelength, we simulate competitive optomechanical coupling rates g_{om} ~800 kHz while achieving spin-mechanical coupling rates g_{sm} ~30 MHz to a spin state of the vacancy complex. Thus, we show that this ultrasmall mode volume device can be used to interact with a vacancy without optically exciting the spin at its native wavelength, operating at the cavity wavelength instead through a optomechanically mediated interaction. Hence, using quantum modeling, we explore utilizing this spin-optomechanical interface for entanglement protocols in quantum networks in a setup depicted in Fig. 1. We use the modeled entanglement rates to feedback on a computer-aided design of an optimized spin-optomechanical interface.

Results

Theory of Spin-Optomechanical Coupling

A spin-optomechanical interface accomplishes two effects. First, it couples the photonic mode of a photonic crystal cavity to the phononic modes of the

[1]Department of Electrical Engineering and Computer Science, Massachusetts Institute of Technology, Cambridge, MA, 02139, USA. [2]University of Massachusetts Amherst, Amherst, MA, 01003, USA. [3]Sandia National Laboratories, Albuquerque, NM, 87185, USA. [4]Wyant College of Optical Sciences, University of Arizona, Tucson, AZ, 85721, USA. [5]DEVCOM Army Research Laboratory, Adelphi, MD, 20783, USA. ✉e-mail: raniwala@mit.edu; englund@mit.edu

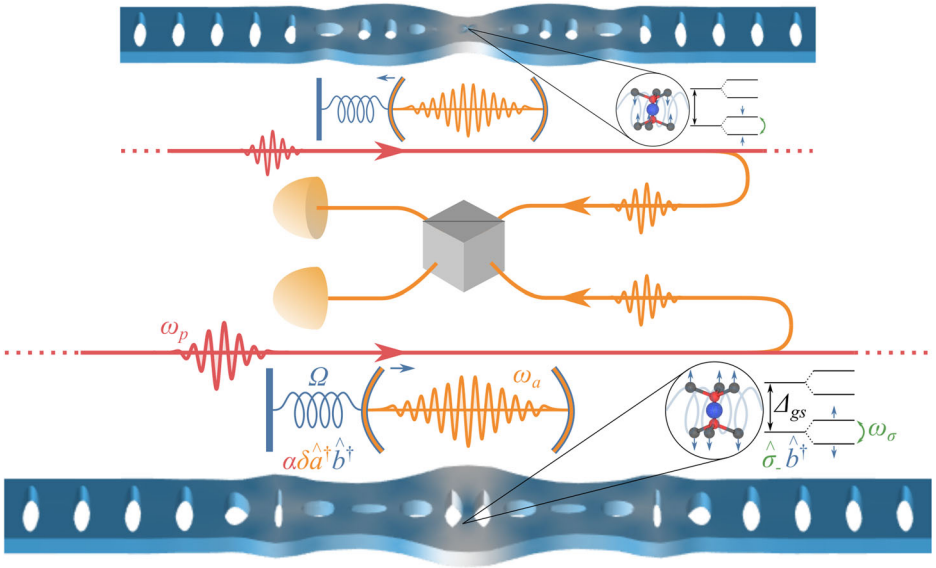

Fig. 1 | Depiction of spin entanglement via a spin-optomechanical interface. Each node contains an optical resonator (orange cavity/operator) coupled to a mechanical resonator (blue spring/operator), with an embedded color center (inset/green operator). A pump (red) is used to induce a two-mode squeezing in the opto-mechanical system. The leakage of an optical photon (orange waveguide) and its detection (orange detector) herald the creation of a single mechanical phonon. A beamsplitter (in gray) can be used to "erase" the knowledge of which is the original source of the photon, leading to the heralding of an entangled state $|10\rangle \pm |01\rangle$ between two neighboring nodes. The phase depends on which of the two detectors clicked[78]. The ground state splitting Δ_{gs} (black) can be actuated with DC strain to selectively detune ω_σ and g_{sm}[23] to turn on and off the spin-phonon interaction and swap the entangled phonon to the spin degree of freedom.

crystal in a pump-driven interaction. Next, it couples the spin transition of a solid-state color center to the same phononic modes. Let us denote the operating frequency of the photonic mode as ω_a, the spin transition frequency as ω_σ between two states of mixed spin–orbit character to permit strain interactions[23], and the pump beam frequency as ω_p. Without loss of generality, we assume only a single phononic mode Ω is nearly resonant with the pump detuning, such that $\Delta = \omega_p - \omega_a \approx \Omega$. Then we can simplify the system Hamiltonian by considering only a single phononic mode. In this picture, the unperturbed Hamiltonian $\hat{H}_0$ can be written as

$$\hat{H}_0 = \hbar\omega_a\hat{a}^\dagger\hat{a} + \hbar\Omega\hat{b}^\dagger\hat{b} + \frac{\hbar\omega_\sigma}{2}\hat{\sigma}_z. \quad (1)$$

Here, $\hat{a}^\dagger, \hat{a}$ and $\hat{b}^\dagger, \hat{b}$ are the ladder operators of the photonic and phononic modes, respectively, and $\hat{\sigma}_j$ is the spin qubit's j-Pauli operator.

Additionally, the parametric coupling between the mechanical and optical resonators takes the form $\hat{H}_{om} = \hbar g_{om}\hat{a}^\dagger\hat{a}(\hat{b}^\dagger + \hat{b})$, i.e., an optical resonance shift dependent on the position of the mechanical resonator. To linearize this interaction, we drive the optical cavity with a pump $\omega_p = \omega_a + \Delta$. By applying the rotating wave approximation and rewriting the photon ladder operators around a mean population $\bar{a}$ as $\hat{a} \to \bar{a} + \hat{a}$, we arrive at the typical optomechanical interaction Hamiltonian in the blue-detuned regime,

$$\hat{H}_{om-bl} = \hbar g_{om}\bar{a}\left(\hat{a}^\dagger\hat{b}^\dagger + \hat{a}\hat{b}\right). \quad (2)$$

In the red-detuned regime, we get the following Hamiltonian

$$\hat{H}_{om-rd} = \hbar g_{om}\bar{a}\left(\hat{a}^\dagger\hat{b} + \hat{a}\hat{b}^\dagger\right). \quad (3)$$

Next we consider the spin–mechanical interaction. In a Group IV diamond defect, spin–strain interactions occur under low static strain and under static magnetic field[17,23,24]. In this regime, the lower branch of the ground manifold weakly mixes with the upper orbital, strain-sensitive states to produce mixed spin–orbit states that are strain susceptible. In the resulting spin–strain interaction picture, the spin-mechanical interaction is generated by deformation-induced strain perturbing the spin states to first order. When the transverse magnetic field experienced by the Group IV defect is such that $\omega_\sigma = \Omega$, this interaction is described by the Hamiltonian

$$\hat{H}_{sm} = \hbar g_{sm}\left(\hat{\sigma}_+\hat{b} + \hat{\sigma}_-\hat{b}^\dagger\right). \quad (4)$$

Here, g_{sm} is the strain-induced coupling by the zero-point fluctuation of the mechanical resonator and $\hat{\sigma_\pm} = \frac{1}{\sqrt{2}}(\sigma_x \pm i\sigma_y)$ (see Supplementary). As such, any phonon excitation will induce zero-point coupling between the spin qubit and resonator phonon and vice versa. In this paper, we assume a static magnetic field around 0.18 T, where the transverse field component relative to the axis of the Group IV defect is sufficiently large such that g_{sm} approaches the strain-orbit coupling term[25]. We will henceforth ignore the upper orbital branch, as well as the optically excited states of the defect, which are far off resonance from the mechanical and/or optical modes of the 1D OMC.

An efficient spin-optomechanical interface requires tuning of couplings g_{om} and g_{sm}, as well as quality factors Q_{opt} and Q_{mech} for a targeted experiment. We delve into the design considerations that affect these parameters below.

Device Simulations

At the core of our proposal is a strain concentrator embedded in a one-dimensional optomechanical crystal (1D OMC) with rectangular cross-section (Fig. 2a). The 1D OMC consists of a nanobeam with periodically etched ellipses, $2n_d$ of which are adiabatically morphed into a defect cell. We then modify the central defect cell by tapering to a width b using a linear taper. This linear taper simultaneously enhances strain by forcing strain energy through the small cross-sectional area of a sharply angled, narrow bridge–as in previous mechanical resonator proposals[22]–and concentrates the optical mode profile–shown in previous photonic crystal designs[26]–in the center of the 1D OMC. In our design, only the central cell is modified with this taper to maximize the interaction of the acoustic phonon with a single spin, as well as the optical field concentration in the same region of concentrating mechanical displacement. We simulate (at $b = 60$ nm, $n_d = 6$) an optical mode of frequency $\omega_a/(2\pi) \approx 200.2$ THz and $Q_{opt} \approx 9.6 \times 10^4$ (Fig. 2f), which lies in the mirror cells' 28.7 THz optical bandgap from 175.28 THz to 203.98 THz (Fig. 2b). We predict an acoustic resonance around $\Omega = 5.39$ GHz (Fig. 2e) between the 2.41 GHz acoustic bandgap from 4.96 GHz to 7.37 GHz (Fig. 2d).

We note here that the parameters governing the defect cell $\{b, a_d, h_{x_d}, h_{y_d}\}$, as well as the crystal orientation in the device α, heavily affect $\{g_{sm}, g_{om}, Q_{opt}\}$ which are critical to the device performance (Q_{mech} is relatively

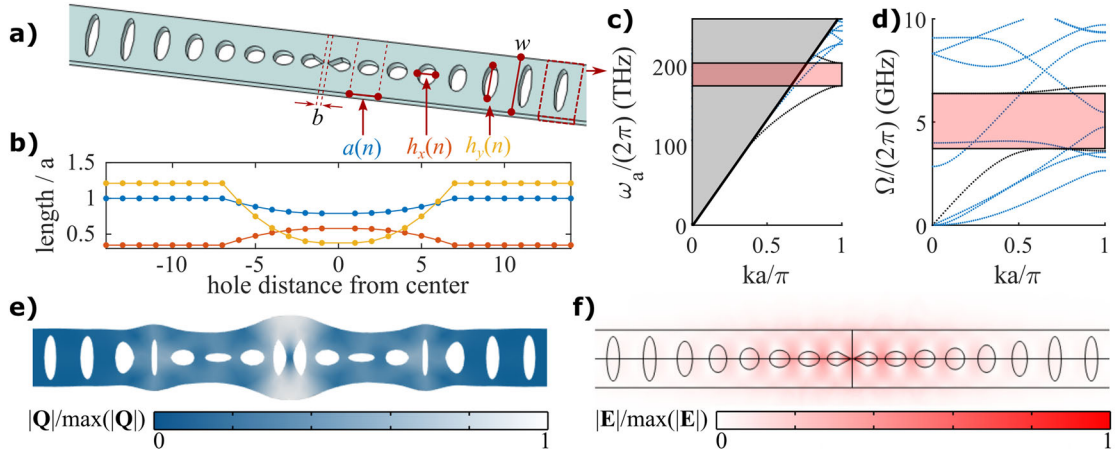

Fig. 2 | Diamond rectangular 1D nanobeam OMC with embedded concentrator, drawing from previous examples in silicon[5,7] and diamond[20,47,79] as well as ultrasmall mode volume photonic and phononic crystals[22,26]. **a** Diagram of the nanobeam photonic crystal. Free parameters include taper width b; unit cell period as a function of cell number n, $a(n)$; unit ellipse width $h_x(n)$ and height $h_y(n)$; and beam width w alongside beam thickness t. **b** Plot of quadratically varying $a(n)$, $h_x(n)$, and $h_y(n)$ on either side of the beam center. This characterizes the cavity parametrized by Table 1 later in the text. **c** optical and (**d**) mechanical bandstructure for the mirror unit cell of the cavity, providing a 28.7 THz bandgap around and a 2.41 GHz mechanical bandgap. **e** mechanical displacement and (**f**) electric field norm profiles of the 5.39 GHz mechanical mode and 200.2 THz optical mode of the cavity. These simulations are for parameters $\{h_{y_d}, h_{x_d}, a_d\} = \{218.2, 334.8, 456.56\}$ nm, $\alpha = 135°$, rest of the parameters are same as from Table 1.

unaffected by the device geometry as long as the phonon frequency Ω lies within the acoustic bandgap, and is rather limited by phonon-thermally and materially-governed phonon–phonon processes[27–30]). As such, we explore the behavior of these performance parameters as a function of the defect unit cell parameters in Fig. 3. From these sweeps, we find a mix of simple and non-trivial relations between the defect cell parameters and the performance parameters. Setting $\alpha = \frac{3\pi}{4}$ rad, for example, maximizes both g_{om} and g_{sm} by simultaneously maximizing the photoelastic contribution to g_{om}–g_{pe}–and the strain along the transverse axis of an emitter in the center of the spin-optomechanical interface.

Additionally, decreasing b, which can be thought of as the spring constant in the central bridge, increases the strain energy density, or equivalently the mechanical mode volume[22], in the central bridge of the spin-optomechanical interface. Intuitively, this can be seen as forcing the same amount of strain energy in the central bridge through a smaller bridge volume. We estimate through FEM that $V_{\mathrm{mech}}/\Lambda_{\mathrm{p}}^3$ and $V_{\mathrm{mech}}/\Lambda_{\mathrm{s}}^3$ drop from $\sim 10^{-4}$ and $\sim 10^{-3}$, respectively, to $\sim 10^{-6}$ and $\sim 10^{-5}$, respectively, as b decreases from 100 nm to 20 nm. Here, Λ_{p} and Λ_{s} are the longitudinal and shear wavelengths in bulk diamond[22]. As V_{mech} decreases, g_{sm} increases, which also increases the "mechanical Purcell enhancement." $V_{\mathrm{opt}}/\lambda^3$ or $V_{\mathrm{opt}}/(\lambda/n)^3$ similarly decrease from $\sim 10^{-2}$ and $\sim 10^{-1}$, respectively, to $\sim 10^{-3}$ and $\sim 10^{-2}$, respectively, with decreasing b–a beneficial effect for simultaneously concentrating the cavity mechanical and optical modes. Here, λ is the free space cavity wavelength, and n is the refractive index of diamond. Practically, we find that both g_{sm} and g_{om} increase as b is made as small as possible, although for $b \leq 20$ nm, the frequency of the mechanical mode (which decreases with decreasing b by the intuitive picture of reducing the 1D OMC spring constant) falls below 4.96 GHz and thus lies outside the acoustic bandgap of the mirror cells. Additionally, fabrication constraints make achieving $b < 20$ nm otherwise challenging. However, the effects of $\{a_d, h_{x_d}, \text{and } h_{y_d}\}$ on the performance parameters are less predictable, owing to a possible interplay between these parameters in the defect cell geometry. In previous studies on optomechanical crystals, these parameters are numerically optimized to yield the best performance parameter set[7]. In this study, which considers a complicated tripartite interface of an optical cavity, a phononic cavity, and an embedded spin system, we would like to motivate the optimization not just by $\{g_{sm}, g_{om}, Q_{opt}, Q_{mech}\}$ but by a protocol that utilizes this interface. We consider non-classical spin state heralding and opto-mechanically mediated entanglement between two spins in the sections below.

Spin-Mediated Entanglement via DLCZ

The controlled opto-mechanical two-mode squeezing represented by Eq. (2) enables us to herald the creation of single phonons in the mechanical resonator. Such excitations can then be deterministically transferred to the spin via the spin-mechanical interaction in Eq. (3) for long term storage. Crucially, if we employ the Duan, Lukin, Cirac, and Zoller's[31,32] entangling protocol, we can herald an entangled $|01\rangle \pm |10\rangle$ state in two remote mechanical resonators. Each of the two mechanical resonators can then deterministically swap its content with their embedded spins by DC strain-actuating the optomechanical crystal to detune the spin from the mechanical mode (see Supplementary), leading to two remote entangled long-lived spins for use in quantum networking.

The DLCZ protocol is, at its core, two single-phonon heralding experiments running in parallel as seen in Fig. 1. However, the detector triggering the heralding is placed after a "path erasure apparatus", e.g., a simple 50–50 beamsplitter. Therefore, when a phonon is heralded by the detection of a photon, the phonon is in equal superposition of being in the left or in the right node. This results in the two mechanical resonators being in the state $|01\rangle \pm |10\rangle$, with the phase depending on which detector clicked. For details on this path erasure consult[31,33].

Hence, we develop a protocol for single-spin heralding by first initializing our spin-phonon system in the ground state via optomechanical cooling and then performing single-phonon heralding and swapping using optomechanical squeezing and spin-swapping. The protocol is shown in Fig. 4a, b, where we (1) cool, (2) herald on the creation of an entangled phonon, and (3) conditionally swap to the vacancy spin state.

We begin by red-sideband optomechanical cooling of the phonon mode with the spin-mechanical coupling on for time $t_B - t_A$. This cools the phonon and coupled spin modes to their ground state. Then we utilize the blue-detuned Hamiltonian to perform the heralding protocol for a time $t_C - t_B$ shorter than the time for the spin or optomechanical cavities to thermally repopulate. After the heralding, the controlled swap operation is implemented depending on if we get a photon click. Then the full system Hamiltonian is

$$\hat{H}_{cool} = \hat{H}_0 + \hat{H}_{\mathrm{om-rd}} + \hat{H}_{\mathrm{sm}}. \tag{5}$$

$$\hat{H}_{herald} = \hat{H}_0 + \hat{H}_{\mathrm{om-bl}} + \hat{H}_{\mathrm{sm}}. \tag{6}$$

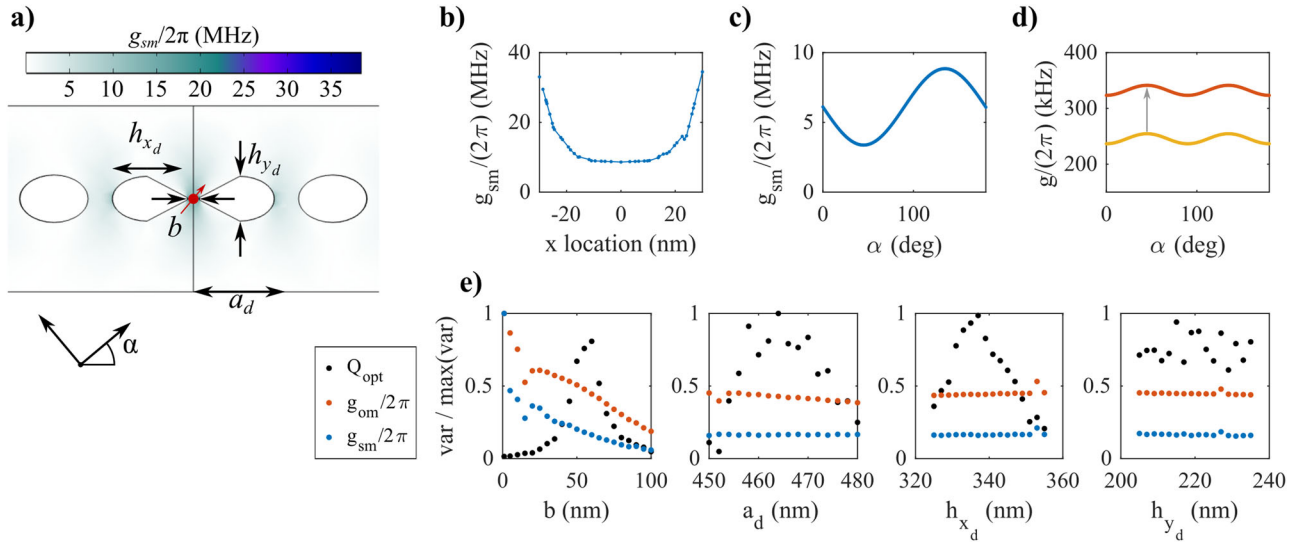

Fig. 3 | Analysis of spin-mechanical coupling profiles and the defect cell parameters that affect this coupling. (**a**) and (**b**) shows the 2D and 1D spin-mechanical coupling g_{sm} profile of the spin-optomechanical crystal breathing mode, with expected position of the Group IV spin overlayed. The parameters b, a_d, h_{x_d}, and h_{y_d} impact the spin-mechanical coupling strength among other variables. The one-dimensional profile in the center of the bridge shows that strain is maximized at the bridge edge but retained in the center away from sidewalls. The crystal axis orientation in the device affects g_{sm} (**c**) and g_{om} (**d**, red) by changing the strain elements the spin sees and the photoelastic effect for g_{pe} (**d**, yellow), which sums with a constant g_{mb} (**d**, gray). **e** Sweeping b, a_d, h_{x_d}, and h_{y_d} about a naive parameter set shows that the parameters governing device performance, namely $\mathrm{var} \in \{Q_{opt}, g_{om}, g_{sm}\}$, are maximized about different variables, motivating protocol-based numerical optimization of the exact design parameters. Q_{mech} was routinely near 10^6 or greater in the sweeps and not depicted. These sweeps are centered around the following parameters $\{h_{y_d}, h_{x_d}, a_d\} = \{220.5, 341.25, 456.75\}$ nm, $\alpha = 135°$; the rest of the parameters are the same as in Table 1.

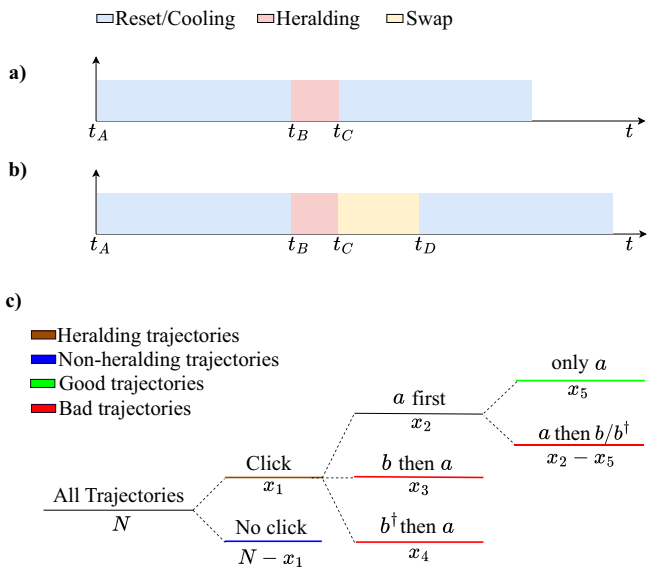

Fig. 4 | Diagram of the full heralding protocol and timing. Schematic of the full protocol depending on the (**a**) absence or (**b**) presence of a photon click on the photo-detectors at $t = t_C$. (**c**) Map of all possible quantum trajectories.We start with N trajectories. Out of them, there is a photon click in x_1 of them. After getting a click, there are three possibilities, where events a, b and b_1 correspond to the three collapse operators described in section 2.3. The spin-phonon swap is performed on all the brown trajectories, but ideally only the green ones are the good trajectories, which means that the red ones, lead to the infidelity of our heralding plus swap protocol. Using the trajectory approach, we can easily estimate, $P_{herald} = \frac{x_1}{N}$ and $p_{good-traj} = \frac{x_5}{x_1}$.

$$\hat{H}_{swap} = \hat{H}_0 + \hat{H}_{\mathrm{sm}}. \tag{7}$$

Below we study the fidelity and success probability of the single-phonon heralding protocol, as its performance directly affects the performance of the overall entanglement protocol. In this process, when writing down kets, we will use the Fock basis of the optical and mechanical modes, written down in that order, e.g., $|01\rangle$ is zero photons and one phonon. Two processes are involved in the single-phonon heralding: the two-mode squeezing in Eq. (6) which leads to the mapping $|00\rangle \to |00\rangle + \varepsilon|11\rangle + \mathcal{O}(\varepsilon^2)$; and the leakage into a waveguide and subsequent detection of the photon, which projects on the $\varepsilon|11\rangle + \mathcal{O}(\varepsilon^2)$ branches. To properly derive the dynamics, we will use a stochastic master equation and we will track the most-probable quantum trajectories manually. The dynamics is governed by the equation

$$\hat{H}_{\mathrm{stoch}} = \hat{H}_0 + \hat{H}_{\mathrm{om-bl}} + \hat{H}_{\mathrm{sm}} - \frac{i}{2}\sum_{c\in\{a,b,b^\dagger\}} \gamma_c \hat{c}^\dagger \hat{c}, \tag{8}$$

where the the sum over jump operators $\hat{c}$ provides a way to track the chance for discontinuous jumps. If $|\psi(t)\rangle$ is the state obtained after evolving $|00\rangle$ under $\hat{H}_{\mathrm{stoch}}$, then the probability density for a jump $\hat{c}$ is $\mathrm{pdf}_c(t) = \gamma_c \frac{\langle\psi(t)|\hat{c}^\dagger\hat{c}|\psi(t)\rangle}{\langle\psi(t)|\psi(t)\rangle}$. The operator $\hat{a}$ represents the chance of photon leakage at rate $\gamma_a = \frac{\omega_a}{Q_{\mathrm{opt}}}$ with Q_{opt} the optical quality factor; $\hat{b}$ corresponds to a phonon leaking to the heat bath at rate $\gamma_b = \frac{\gamma_m(n_{\mathrm{th}}+1)}{2}$, where $\gamma_m = \frac{2\Omega}{Q_{\mathrm{mech}}}$ with Q_{mech} the quality factor of the mechanical resonator (notice the different convention leading to a factor of 2 difference); lastly $\hat{b}^\dagger$ corresponds to receiving a phonon from the bath at rate $\gamma_{b^\dagger} = \frac{\gamma_m n_{\mathrm{th}}}{2}$, where $n_{\mathrm{th}} = \frac{k_b\tau}{\Omega}$ is the average number of phonons in the bath, k_b is the Boltzman constant, and τ is the temperature of the bath. Solving for the dynamics and the probability densities of various jumps, as done in details in the interactive supplementary materials[34] leads to:

1. To zeroth order, no jump occurs.
2. To first order, a photon–phonon pair is heralded. The probability of that event is $P_a = \int_0^T \mathrm{d}t \mathrm{pdf}_a(t)$.
3. To second order, a photon–phonon pair is heralded and then followed by any other event, for an overall of probability $P_{a^*} = 1 - \langle\psi(T)|\psi(T)\rangle$.
4. Also to second order, a b event at time τ is followed by an a event, happening with $P_{ba} = \int_0^T \mathrm{d}\tau\, \mathrm{pdf}_b(\tau) \int_\tau^T \mathrm{d}t\, \mathrm{pdf}_{ba}(t)$.
5. Similarly for $b^\dagger$ followed by a we have probability $P_{b^\dagger a}$.

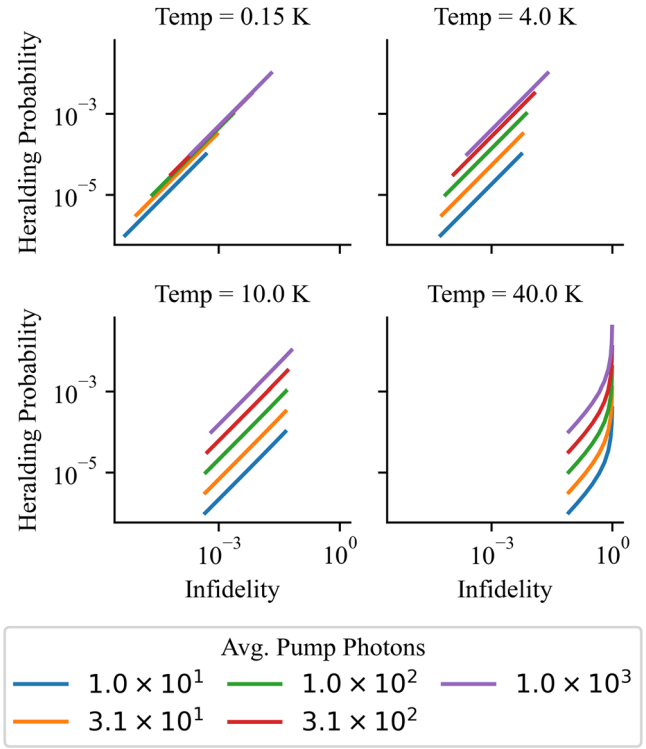

Fig. 5 | Heralding probability and single-phonon infidelities as a function of temperature (facet) and pump power (color), parameterized by pump pulse duration (each line spans $T = T_a$ to $T = 10^3 T_a$). Shorter pulses have lower probability and infidelity. However, the rate of heralding is independent of T as the shorter the pulse (the higher the repetition rate), the lower the heralding probability for that attempt is. Therefore short pump pulses are preferable as that leads to lower infidelity. In this setup, at $\tau = 40K$, $\alpha = \sqrt{1000}$, and $T = T_a$, we can theoretically achieve rates of successful single-phonon heralding in the tens of kHz at infidelity lower than 10%. The performance is even better at lower temperatures. At around $4K$ we see that the detrimental effects from the bath of the mechanical resonator become negligible compared to the infidelity due to multi-phonon excitations.

Above, T is the duration of the pump pulse. These are all the branches of the dynamics that have a chance of triggering a heralding event (to leading order). The total chance for heralding is $P = P_a + P_{ba} + P_{b^\dagger a}$, while the fidelity of the heralded single phonon is $F = \frac{P_a - P_{a*}}{P_a + P_{ba} + P_{b^\dagger a}} f_0$, where $f_0 = \langle 1|\rho_a|1\rangle$ is the fidelity of "good heralding" branch of the dynamics. ρ_a is the density matrix for the state conditioned on only one a event having happened during the pump pulse of duration T. The above trajectories can be seen pictorially in Fig. 4c.

After simplifying and taking into account that the decay of the optical cavity is much faster than the optomechanical interaction ($T_a = \gamma_a^{-1} \ll (\bar{a} g_{OM})^{-1}$), we obtain:

$$P = 4\bar{a}^2 g_{\mathrm{om}}^2 T_a T, \tag{9}$$

$$1 - F = 8\bar{a}^2 g_{\mathrm{om}}^2 T_a T + \frac{3}{4}\gamma_m T_a T\left(3n_{\mathrm{th}} + 1\right). \tag{10}$$

Notice the term in the infidelity that scales exactly as the heralding probability: This is due to the $(\mathcal{O})(\varepsilon^2)$ next-to-leading-order effect in the two-mode squeezing, leading to a proportionally larger chance of more-than-one excitations being heralded. There is also a second term, purely related to the detrimental effects of the thermal bath on the mechanical resonator. As long as $k_b \tau \ll Q_{\mathrm{mech}} \alpha^2 g_{\mathrm{om}}^2$ we can neglect the bath heating term, however this can be difficult to quantify as Q_{mech} strongly depends on τ. This transition between leading sources of infidelity can be seen in Fig. 5.

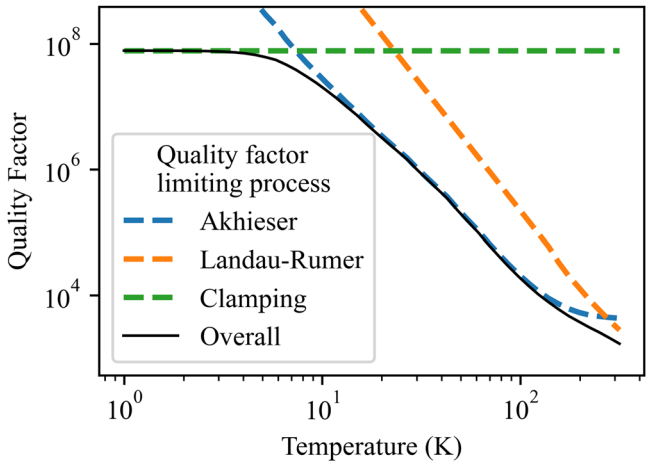

Fig. 6 | The processes limiting the quality factor of a mechanical resonator. At low temperature only clamping losses matter (green), but past a certain temperature Akhieser (blue) and Landau-Rumer (orange) processes dominate. These estimates depend on thermal properties of bulk diamond as reported in the literature. Thin-sheet diamond, as used in our devices, can have slightly differing properties.

These are the heralding probability and fidelity of a single phononic excitation. The heralding probability and fidelity for the complete entangling protocol, in which two nodes are pumped in parallel and the photon is looked for only after "path-information erasure" differ. To leading order, the probability $P_e = 2P$ is twice as high as either node can produce a photon, and the infidelity scales the same.

For long term storage, we coherently swap the phononic excitation into the spin. The swap gate contributes an additional infidelity of $n_{\mathrm{th}}\gamma_m/g_{\mathrm{sm}}$ which is much lower than other sources of infidelity.

These results, given the design parameters of the previous section, are detailed in Fig. 5. Of note is that Q_{mech} is very strongly dependent on the bath temperature due to scattering processes among the thermal phonons. At low temperatures, only clamping losses due to the design of the resonator are of importance, but as the temperature increases, Akhieser and then Landau-Rumer processes become important[35–38]. The typical dependence for our design and material parameters can be seen in Fig. 6. The Akhieser limited quality factor is $Q_A = \frac{1}{\Omega\tau}\frac{\rho c^4}{2\pi\gamma^2\kappa}$, where ρ is density, c is speed of light, γ is the Grüneisen coefficient, and κ is the thermal conductivity. Only κ depends strongly on temperature, and we use the values reported in[39–44]. At even higher temperature the Landau-Rumer processes dominate with $Q_{LR} = \frac{2\rho c^2}{\pi\gamma^2 C_v \tau}$, where C_v is the diamond heat capacity as reported in[45,46].

Thus, with our design we can theoretically achieve single-phonon generation at tens of kHz and infidelity lower than 10% at temperature $\tau = 40\ K$, number of photons in the pump mode $\alpha^2 = 1000$, pump pulse duration $T = T_a$. At lower temperatures the performance significantly improves, giving limiting infidelities far below 1%.

Quantum Monte Carlo verification and Design Feedback

Finally, we use the protocol above to feedback on the optomechanical crystal design parameters (namely, a_d, h_{x_d}, and h_{y_d}) (Fig. 7a, b) to minimize the cost-function which is a function of fidelity and rate of heralding (see Supplementary). We verify the theoretical equations Eq. (9) and Eq. (10) using a quantum monte-carlo approach (see Supplementary) and proceed to use a COMSOL-to-Python (theory + quantum master equation) feedback loop to optimize the crystal design.

We select a bridge width b of 60 nm, taking into account the nanofabrication considerations, and defect unit cell number n_d as 6. Starting with the free variables h_{y_d}, h_{x_d}, and a_d, we run our Bayesian optimization routine (described in Supplementary Section 5.4). We run a COMSOL finite element method (FEM) simulation to extract device parameters $\{\omega_a, \Omega, Q_{opt}, Q_{mech}, g_{om}, g_{sm}\}$ as described in Section 2.1 and 2.2. The COMSOL simulation is interfaced with python API using the MPh module, which for each

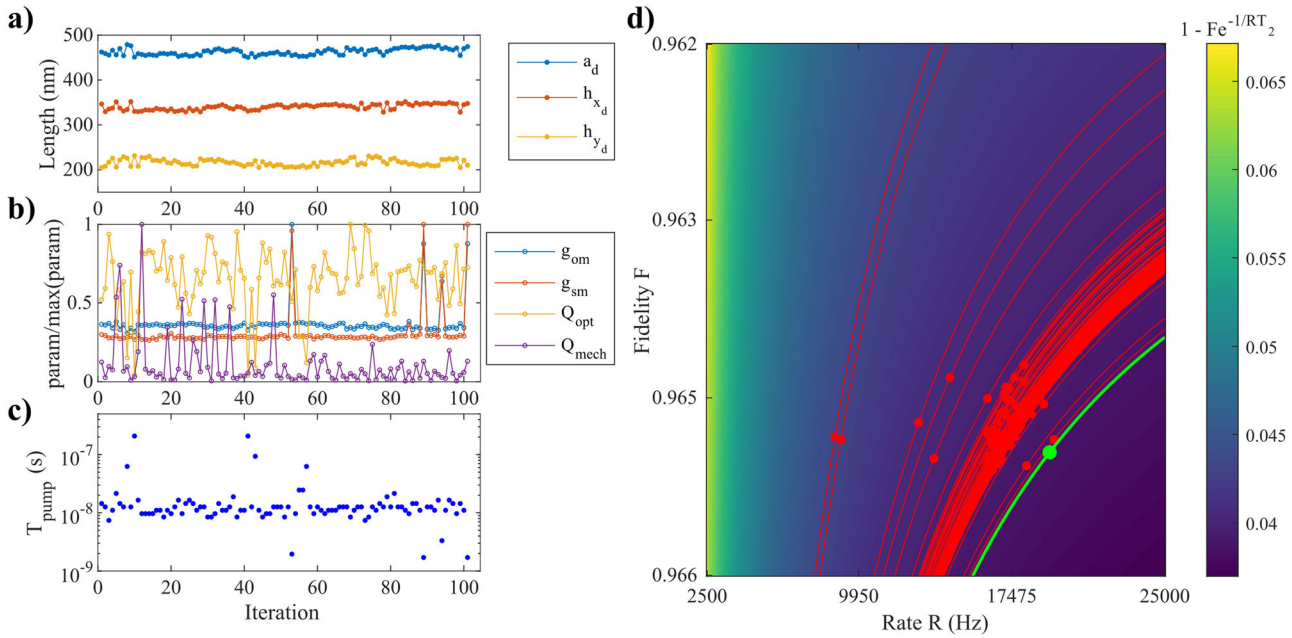

Fig. 7 | Design feedback using FEM-QuTiP optimization. (**a**) Shows the change in a_d, h_{x_d}, and h_{y_d} at each Bayesian optimizer iteration, where the resulting performance parameter variation is shown in (**b**). For each iteration of $\{a_d, h_{x_d}, h_{y_d}\}$, optimizer individually selects an optimum pump time T_{pump} which minimizes the cost function for that iteration and (**c**) shows the change in T_{pump} by iteration. (**d**) Shows the rate-fidelity tradeoff of the cost function at each iteration (red), with the optimized point highlighted (green). The red (green) lines represent curves in the rate-fidelity space with equal cost function to the iteration points.

Table 1 | Spin-optomechanical cavities optimized by the FEM-QuTiP optimization in Quantum Monte Carlo verification and Design Feedback

Mat.	Emitters	a	a_d	h_x	h_{x_d}	h_y	h_{y_d}	w	t	b	Q_{opt}	Q_{mech}	$g_{om}/2\pi$ (Hz)
Dmd	SiV^-	577.5	474.5	200	347.7	700	210.1	913.5	250	60	8.6e4	6.2e7	8.2e5
SiC	V_{Si}^-	480	299.6	235	230	600	340.4	750	250	60	2.8e3	2.0e6	1.9e6
Si	Si:B	535	435	325	342.9	370	305	500	220	60	6.37e3	2.1e6	3.7e6

The emitter used in the optimization protocol is listed next to each material.
All parameters $\{a, a_d, h_x, h_{x_d}, h_y, h_{y_d}, w, t, b\}$ are listed in nm. For these optimizer runs, we assumed a temperature of 100 mK, and a T_2 of 13 ms[59], 1 ms[60] and 0.9 ms[61], for SiV^-, V_{Si}^- and Si:B respectively.

iteration transfers the COMSOL results to QuTiP. This then evaluates the heralding success rate and fidelity for the protocol described in Section 2.3 (see Supplement for more details). After evaluating the cost-function (CF) for the protocol ($C(F, R, T_2) = 1 - Fe^{-1/RT_2}$), we proceed to next iteration. Fig. 7a shows how the optimizer updates the variables h_{y_d}, h_{x_d}, a_d through each iteration. Fig. 7b shows the variation of $\{g_{om}, g_{sm}, Q_{opt}, Q_{mech}\}$ with progressive iterations. T_{pump} acts like a hyperparameter such that for each iteration, the optimizer selects the value of T_{pump} which minimizes the CF for that iteration (shown in Fig. 7c). Figure 7d shows the optimization trajectory in Fidelity-Rate tradespace with the optimum fidelity ~ 0.96 and rate ~ 20 kHz. Through this optimization, we arrive at a final design parameter set in Table 1.

Possible improvements to the protocol include (1) spectral and spatial multiplexing (2) use of a Dicke state of multiple nearby color centers to enhance g_{sm} (3) use the nuclear registers for even longer storage times (4) entanglement purification with the nuclear registers which greatly increase the entanglement fidelity while only marginally decreasing the entanglement rate.

Discussion

In this paper, we bring the idea of a self-similar concentrator from photonic crystal devices[26] to a 1D optomechanical crystal and explore the usage of the resulting cavity in spin-optomechanical interfacing. This system poses the advantages afforded by highly concentrated optical and mechanical modes: high strain in a central region while retaining optomechanical coupling in diamond relative to previously proposed and demonstrated devices[47], and thus strong spin–phonon interactions. From FEM simulations, we demonstrate that this spin-optomechanical interface can achieve 820 kHz single photon–phonon coupling alongside 32 MHz spin–phonon coupling to a Group IV spin. The strength of this spin–phonon interaction is such that we can effectively ignore losses incurred when swapping a quantum between a cavity phonon and the spin state.

We explore implementation of our interface in an optically heralded entanglement protocol[31,33]. In this scheme, identical cavities are entangled via heralding, and the resulting entangled phonons are swapped into their respective coupled spins. This entanglement procedure completely circumvents standard issues related to spin-addressing, including the need to operate at the emitter's optical transition wavelength (we define the optical wavelength with a telecom photonic mode) and concerns related to spectral diffusion of emitters (we never optically excite the emitter). Additionally, this scheme places no strong requirements on the optical quality factors required by other works to accomplish spin-mechanical addressing[48,49]–instead operating with low optical Qs to increase the rate of heralding–and requires on-chip devices that are well within fabricable parameters.

Our spin-optomechanical architecture applies to other material platforms besides diamond. For example, silicon (Si) and silicon carbide (SiC)

Table 2 | Spin defect candidates for optomechanical interfacing

Defect	Material	$g_{sm_{proj}}/2\pi$	~ T_1 (@T)	~ T_2(@T)
SiV^-	Diamond	~ 32 MHz	0.1 ms @40 mK[62]	0.2 ms @40 mK[62]
SnV^-	Diamond	~ 26 MHz	10 ms @3K[63]	0.3 ms @1.7K[64]
NV^-	Diamond	~ 440 Hz	100 s @20K[65]	0.6 s @77K[66]
Si:B	Si	~ 30 MHz	7.4 μs @45mK[19,67]	2.6 μs @45mK[19,67]
Si:P	Si	~ 70 MHz	0.3 s @7K[68]	60 ms @7K[68]
V_{Si}	SiC	~ 10 MHz	10 s @17K[69]	20 ms @17K[69]
VV^0_{Si}	SiC	~ 2 kHz	8 ms @20K[70]	1 ms @20K[71]

The defects and their host materials, projected couplings $g_{sm_{proj}}$, and measured T_1 and T_2 at different operating temperatures are listed.

The $g_{sm_{proj}}$ of the SnV^-, NV^-, V_{Si}, and VV^0_{Si} were estimated by modifying parameters in the SiV^- coupling formula[63,72–76]. The B:Si and P:Si $g_{sm_{proj}}$ were estimated by substituting our $b = 60$ nm mode volume into the formulae in[19] and[77], respectively. The defect naming conventions have been copied from references.

have been used for optomechanics[5,7,50–53] and have quantum emitters including carbon-based T-centers, phosphorus vacancies, and boron impurities[19,54]. In particular, Si with B:Si acceptor impurities has been considered for operating spin-phonon coupled systems as an acoustic alternative to circuit-cavity QED[19]. Here, we have shown that with an intentionally designed optomechanical cavity, one can achieve g_{sm} much larger than previously proposed–which should be the case irrespective of the material, whether diamond, silicon, or another alternative–alongside respectable g_{om}, such that the full spin-optomechanical interface's performance can be evaluated (see Table 2). We have analyzed this interface assuming a SiV^- spin, which has well-documented spin-strain parameters[17,23]; however the spin-dephasing time is highly limited above single-Kelvin temperatures due to electron-phonon dephasing[55]. As such, future works may use this spin-optomechanical framework while selecting a suitable combination of material platform and temperature-robust, highly strain-tunable spin defect. The beauty of this platform is that, given sideband-resolved cooling of nanomechanical oscillators at a few Kelvin[56] or ~20 K[57], quantum operation of a solid-state spin would not be limited by optical lifetimes and instead enabled by state-of-the-art optomechanics. The ability to separately engineer quantum memories and spin-photon interfaces, while retaining efficient interfacing between them even at moderate temperatures up to 40 K, will provide much-needed design freedom in applications from quantum networks to computing to sensing. Our COMSOL file, code for COMSOL-python optimizer, QuTiP simulation can be found in our GitHub repository[58].

Methods

We conduct FEM-and-QuTiP optimization using COMSOL Multiphysics 5.4 and the QuTiP package in Python. We run electromagnetic (EM) FEM simulations using a COMSOL-Python API to determine the optical mode properties of the optomechanical crystal. We perform structural mechanics (SM) FEM simulation through the COMSOL-Python API to determine the mechanical modes of the system. We feed the FEM simulation results into custom QuTiP code for estimating entanglement rate and fidelity. Finally, we feed the FEM and QuTiP steps into a built-in SciPy Bayesian optimizer for up to 100 iterations to optimize the optomechanical crystal parameters.

Data availability

Data are available upon reasonable request. Please refer to Hamza Raniwala at raniwala@mit.edu.

Code availability

The code used to conduct this research is available at https://github.com/panand2257/Spin_Optomechanical_Interf aces.

Received: 19 September 2024; Accepted: 18 February 2025;
Published online: 14 July 2025

References

1. Kepler, J. *De cometis libelli tres* (Typis Andre Apergeri, sumptibus Sebastiani Mylii, bibliopol Augustani, 1619).
2. Aspelmeyer, M., Kippenberg, T. J. & Marquardt, F. *Cavity optomechanics: nano-and micromechanical resonators interacting with light* (Springer, 2014).
3. Ashkin, A. Trapping of atoms by resonance radiation pressure. *Phys. Rev. Lett.* **40**, 729 (1978).
4. Cuthbertson, B., Tobar, M., Ivanov, E. & Blair, D. Parametric back-action effects in a high-q cyrogenic sapphire transducer. *Rev. Sci. Instrum.* **67**, 2435–2442 (1996).
5. Eichenfield, M., Chan, J., Camacho, R. M., Vahala, K. J. & Painter, O. Optomechanical crystals. *Nature* **462**, 78–82 (2009).
6. Eichenfield, M., Camacho, R., Chan, J., Vahala, K. J. & Painter, O. A picogram-and nanometre-scale photonic-crystal optomechanical cavity. *Nature* **459**, 550–555 (2009).
7. Chan, J., Safavi-Naeini, A. H., Hill, J. T., Meenehan, S. & Painter, O. Optimized optomechanical crystal cavity with acoustic radiation shield. *Appl. Phys. Lett.* **101**, 081115 (2012).
8. Wilson-Rae, I., Nooshi, N., Zwerger, W. & Kippenberg, T. J. Theory of ground state cooling of a mechanical oscillator using dynamical backaction. *Phys. Rev. Lett.* **99**, 093901 (2007).
9. Vainsencher, A., Satzinger, K., Peairs, G. & Cleland, A. Bi-directional conversion between microwave and optical frequencies in a piezoelectric optomechanical device. *Appl. Phys. Lett.* **109**, 033107 (2016).
10. Mirhosseini, M. et al. Superconducting qubit to optical photon transduction. *Nature* **588**, 599–603 (2020).
11. Forsch, M. et al. Microwave-to-optics conversion using a mechanical oscillator in its quantum ground state. *Nat. Phys.* **16**, 69–74 (2020).
12. Jiang, W. et al. Efficient bidirectional piezo-optomechanical transduction between microwave and optical frequency. *Nat. Commun.* **11**, 1–7 (2020).
13. Wu, M., Zeuthen, E., Balram, K. C. & Srinivasan, K. Microwave-to-optical transduction using a mechanical supermode for coupling piezoelectric and optomechanical resonators. *Phys. Rev. Appl.* **13**, 014027 (2020).
14. Riedinger, R. et al. Remote quantum entanglement between two micromechanical oscillators. *Nature* **556**, 473–477 (2018).
15. Zhong, C., Han, X., Tang, H. X. & Jiang, L. Entanglement of microwave-optical modes in a strongly coupled electro-optomechanical system. *Phys. Rev. A* **101**, 032345 (2020).
16. Childress, L. I. *Coherent manipulation of single quantum systems in the solid state* (Harvard University, 2007).
17. Hepp, C. et al. Electronic structure of the silicon vacancy color center in diamond. *Phys. Rev. Lett.* **112**, 036405 (2014).
18. Wolfowicz, G. et al. Quantum guidelines for solid-state spin defects. *Nat. Rev. Mater.* **6**, 906–925 (2021).
19. Ruskov, R. & Tahan, C. On-chip cavity quantum phonodynamics with an acceptor qubit in silicon. *Phys. Rev. B* **88**, 064308 (2013).
20. Maity, S. et al. Coherent acoustic control of a single silicon vacancy spin in diamond. *Nat. Commun.* **11**, 1–6 (2020).
21. Shandilya, P. K., Lake, D. P., Mitchell, M. J., Sukachev, D. D. & Barclay, P. E. Optomechanical interface between telecom photons and spin quantum memory. 2102.04597 (2021).
22. Schmidt, M. K., Poulton, C. G. & Steel, M. J. Acoustic diamond resonators with ultrasmall mode volumes. *Phys. Rev. Res.* **2**, 033153 (2020).
23. Meesala, S. et al. Strain engineering of the silicon-vacancy center in diamond. *Phys. Rev. B* **97**, 205444 (2018).
24. Neuman, T. et al. A phononic interface between a superconducting quantum processor and quantum networked spin memories. *npj Quantum Inf.* **7**, 121 (2021).

25. Raniwala, H. et al. Spin-phonon-photon strong coupling in a piezomechanical nanocavity https://arxiv.org/abs/2202.11291 (2022).
26. Choi, H., Heuck, M. & Englund, D. Self-similar nanocavity design with ultrasmall mode volume for single-photon nonlinearities. *Phys. Rev. Lett.* **118**, 223605 (2017).
27. Akhiezer, A. On the absorption of sound in solids. *J. Phys. (Mosc.)* **1**, 277–287 (1961).
28. Landau, L. D. & Rumer, Y. B. Absorption of sound in solids. *Phys. Z. Sowjetunion* **11** (1937).
29. Woodruff, T. O. & Ehrenreich, H. Absorption of sound in insulators. *Phys. Rev.* **123**, 1553–1559 (1961).
30. Tabrizian, R., Rais-Zadeh, M. & Ayazi, F. Effect of phonon interactions on limiting the f.q product of micromechanical resonators. In *TRANSDUCERS 2009 - 2009 International Solid-State Sensors, Actuators and Microsystems Conference*, 2131–2134 (2009).
31. Duan, L.-M., Lukin, M. D., Cirac, J. I. & Zoller, P. Long-distance quantum communication with atomic ensembles and linear optics. *Nature* **414**, 413–418 (2001).
32. Krastanov, S. et al. Optically heralded entanglement of superconducting systems in quantum networks. *Phys. Rev. Lett.* **127**, 040503 (2021).
33. Krastanov, S. et al. Optically-heralded entanglement of superconducting systems in quantum networks 2012.13408 (2021).
34. Krastanov, S. Optomechanics two-mode squeezing and single phonon heralding https://doi.org/10.5281/zenodo.5855089 (2022).
35. Ghaffari, S. et al. Quantum limit of quality factor in silicon micro and nano mechanical resonators. *Sci. Rep.* **3**, 1–7 (2013).
36. Duwel, A., Candler, R. N., Kenny, T. W. & Varghese, M. Engineering mems resonators with low thermoelastic damping. *J. microelectromechanical Syst.* **15**, 1437–1445 (2006).
37. Kunal, K. & Aluru, N. Akhiezer damping in nanostructures. *Phys. Rev. B* **84**, 245450 (2011).
38. Maris, H. J. Interaction of sound waves with thermal phonons in dielectric crystals. In *Physical Acoustics*, vol. 8, 279–345 (Elsevier, 1971).
39. Technology, D. M. A. D. *The CVD diamond booklet* (Diamond Materials: Advanced Diamond Technology, www.diamond-materials.com/download 2021).
40. Pohl, R. The applicability of the debye model to thermal conductivity. *Z. f. ür. Phys.* **176**, 358–369 (1963).
41. Berman, R., Simon, F. E. & Ziman, J. M. The thermal conductivity of diamond at low temperatures. *Proc. R. Soc. Lond. Ser. A. Math. Phys. Sci.* **220**, 171–183 (1953).
42. Pan, L. S. & Kania, D. R.*Diamond: Electronic Properties and Applications: Electronic Properties and Applications*, vol. 294 (Springer Science & Business Media, 1994).
43. Barman, S. & Srivastava, G. Temperature dependence of the thermal conductivity of different forms of diamond. *J. Appl. Phys.* **101**, 123507 (2007).
44. Graebner, J. & Herb, J. Dominance of intrinsic phonon scattering. *Diamond Films and Technology* **1** (1992).
45. Reeber, R. R. & Wang, K. Thermal expansion, molar volume and specific heat of diamond from 0 to 3000k. *J. Electron. Mater.* **25**, 63–67 (1996).
46. Corruccini, R. J. & Gniewek, J. J. *Specific Heats and Enthalpies of Technical Solids at Low Temperatures: A Compilation from the Literature*, vol. 21 (US Government Printing Office, 1960).
47. Burek, M. J. et al. Diamond optomechanical crystals. *Optica* **3**, 1404–1411 (2016).
48. Ji, J.-W. et al. Proposal for room-temperature quantum repeaters with nitrogen-vacancy centers and optomechanics. *arXiv preprint arXiv:2012.06687* (2020).
49. Ghobadi, R., Wein, S., Kaviani, H., Barclay, P. & Simon, C. Progress toward cryogen-free spin-photon interfaces based on nitrogen-vacancy centers and optomechanics. *Phys. Rev. A* **99**, 053825 (2019).
50. Ren, H. et al. Two-dimensional optomechanical crystal cavity with high quantum cooperativity. *Nat. Commun.* **11**, 1–10 (2020).
51. Lu, X., Lee, J. Y. & Lin, Q. High-frequency and high-quality silicon carbide optomechanical microresonators. *Sci. Rep.* **5**, 1–9 (2015).
52. Lu, X., Lee, J. Y., Rogers, S. D. & Lin, Q. Silicon carbide double-microdisk resonator. *Opt. Lett.* **44**, 4295–4298 (2019).
53. Lu, X., Lee, J. Y. & Lin, Q. Silicon carbide zipper photonic crystal optomechanical cavities. *Appl. Phys. Lett.* **116**, 221104 (2020).
54. Bergeron, L. et al. Silicon-integrated telecommunications photon-spin interface. *PRX Quantum* **1**, 020301 (2020).
55. Jahnke, K. D. et al. Electron–phonon processes of the silicon-vacancy centre in diamond. *N. J. Phys.* **17**, 043011 (2015).
56. Qiu, L., Shomroni, I., Seidler, P. & Kippenberg, T. J. Laser cooling of a nanomechanical oscillator to its zero-point energy. *Phys. Rev. Lett.* **124**, 173601 (2020).
57. Chan, J. et al. Laser cooling of a nanomechanical oscillator into its quantum ground state. *Nature* **478**, 89–92 (2011).
58. Anand, P. Codes. https://github.com/panand2257/Spin_Optomechanical_Interfaces (2024).
59. Sukachev, D. D. et al. Silicon-vacancy spin qubit in diamond: a quantum memory exceeding 10 ms with single-shot state readout. *Phys. Rev. Lett.* **119**, 223602 (2017).
60. Fazio, T., Deretzis, I., Fisicaro, G., Paladino, E. & La Magna, A. Stability and decoherence analysis of the silicon vacancy in 3*c*-SiC. *Phys. Rev. A* **109**, 022603 (2024).
61. Kobayashi, T. et al. Engineering long spin coherence times of spin–orbit qubits in silicon. *Nat. Mater.* **20**, 38–42 (2021).
62. Becker, J. N. et al. All-optical control of the silicon-vacancy spin in diamond at millikelvin temperatures. *Phys. Rev. Lett.* **120**, 053603 (2018).
63. Trusheim, M. E. et al. Transform-limited photons from a coherent tin-vacancy spin in diamond. *Phys. Rev. Lett.* **124**, 023602 (2020).
64. Debroux, R. et al. Quantum control of the tin-vacancy spin qubit in diamond. *Phys. Rev. X* **11**, 041041 (2021).
65. Jarmola, A., Acosta, V. M., Jensen, K., Chemerisov, S. & Budker, D. Temperature- and magnetic-field-dependent longitudinal spin relaxation in nitrogen-vacancy ensembles in diamond. *Phys. Rev. Lett.* **108**, 197601 (2012).
66. Bar-Gill, N., Pham, L. M., Jarmola, A., Budker, D. & Walsworth, R. L. Solid-state electronic spin coherence time approaching one second. *Nat. Commun.* **4**, 1–6 (2013).
67. Song, Y. & Golding, B. Manipulation and decoherence of acceptor states in silicon. *Europhys. Lett.* **95**, 47004 (2011).
68. Tyryshkin, A. M., Lyon, S. A., Astashkin, A. V. & Raitsimring, A. M. Electron spin relaxation times of phosphorus donors in silicon. *Phys. Rev. B* **68**, 193207 (2003).
69. Simin, D. et al. Locking of electron spin coherence above 20 ms in natural silicon carbide. *Phys. Rev. B* **95**, 161201 (2017).
70. Falk, A. L. et al. Polytype control of spin qubits in silicon carbide. *Nat. Commun.* **4**, 1819 (2013).
71. Christle, D. J. et al. Isolated electron spins in silicon carbide with millisecond coherence times. *Nat. Mater.* **14**, 160–163 (2015).
72. Ovartchaiyapong, P., Lee, K. W., Myers, B. A. & Jayich, A. C. B. Dynamic strain-mediated coupling of a single diamond spin to a mechanical resonator. *Nat. Commun.* **5**, 4429 (2014).
73. Teissier, J., Barfuss, A., Appel, P., Neu, E. & Maletinsky, P. Strain coupling of a nitrogen-vacancy center spin to a diamond mechanical oscillator. *Phys. Rev. Lett.* **113**, 020503 (2014).
74. Whiteley, S. J. et al. Spin–phonon interactions in silicon carbide addressed by gaussian acoustics. *Nat. Phys.* **15**, 490–495 (2019).
75. Udvarhelyi, P. et al. Vibronic states and their effect on the temperature and strain dependence of silicon-vacancy qubits in 4*h*-SiC. *Phys. Rev. Appl.* **13**, 054017 (2020).
76. Udvarhelyi, P. & Gali, A. Ab initio spin-strain coupling parameters of divacancy qubits in silicon carbide. *Phys. Rev. Appl.* **10**, 054010 (2018).

77. Soykal, O. O., Ruskov, R. & Tahan, C. Sound-based analogue of cavity quantum electrodynamics in silicon. *Phys. Rev. Lett.* **107**, 235502 (2011).
78. Barrett, S. D. & Kok, P. Efficient high-fidelity quantum computation using matter qubits and linear optics. *Physical Review A* **71** (2005).
79. Cady, J. V. et al. Diamond optomechanical crystals with embedded nitrogen-vacancy centers. *Quantum Sci. Technol.* **4**, 024009 (2019).

Acknowledgements

We would like to thank Gerry Gilbert and Gen Clark for insightful comments on this research. The Julia and Python open source communities provided invaluable research software. The hardware design was done in COMSOL. S.K. and H.R. are grateful for the funding provided by the MITRE Quantum Moonshot Program. H.R. acknowledges support from the NDSEG Fellowship and the NSF Center for Ultracold Atoms. P.A. acknowledges support from the Center for Quantum Networks. M.E. performed this work, in part, at the Center for Integrated Nanotechnologies, an Office of Science User Facility, operated for the US Department of Energy Office of Science. D.E. acknowledges support from NSF. D.E. holds shares in Quantum Network Technologies.

Author contributions

H.R., P.A., S.K., and D.E. conceived of the research. H.R. designed the spin-optomechanical crystal interface and developed the COMSOL simulations for the optomechanical crystal. P.A. wrote the FEM-QuTiP optimization code in Python and generated the optimization results. S.K. wrote theory for the photon-photon entanglement for two spin-optomechanical interfaces. M.E., M.T., and D.E. provided supervision and guidance during the project.

Competing interests

D.E. holds shares in Quantum Network Technologies. The remaining authors declare no competing interests.

Additional information

Supplementary information The online version contains supplementary material available at https://doi.org/10.1038/s41534-025-00999-x.

Correspondence and requests for materials should be addressed to Hamza Raniwala or Dirk R. Englund.